J. Fluid Mech. (2024), *vol*. 992, R2, doi:10.1017/jfm.2024.748

The effect of Reynolds number on the separated flow over a low-aspect-ratio wing

Luke Smith[1],† **and Kunihiko Taira**[1]

[1]Department of Mechanical and Aerospace Engineering, University of California, Los Angeles, CA 90095, USA

(Received 16 July 2024; revised 31 July 2024; accepted 5 August 2024)

At high incidence, low-aspect-ratio wings present a unique set of aerodynamic characteristics, including flow separation, vortex shedding and unsteady force production. Furthermore, low-aspect-ratio wings exhibit a highly impactful tip vortex, which introduces strong spanwise gradients into an already complex flow. In this work, we explore the interaction between leading-edge flow separation and a strong, persistent tip vortex over a Reynolds number range of $600 \leq Re \leq 10\,000$. In performing this study, we aim to bridge the insight gained from existing low-Reynolds-number studies of separated flow on finite wings ($Re \approx 10^2$) and turbulent flows at higher Reynolds numbers ($Re \approx 10^4$). Our study suggests two primary effects of the Reynolds number. First, we observe a break from periodicity, along with a dramatic increase in the intensity and concentration of small-scale eddies, as we shift from $Re = 600$ to $Re = 2500$. Second, we observe that many of our flow diagnostics, including the time-averaged aerodynamic force, exhibit reduced sensitivity to Reynolds number beyond $Re = 2500$, an observation attributed to the stabilising impact of the wing tip vortex. This latter point illustrates the manner by which the tip vortex drives flow over low-aspect-ratio wings, and provides insight into how our existing understanding of this flow field may be adjusted for higher-Reynolds-number applications.

Key words: vortex dynamics, wakes, separated flows

1. Introduction

Low-aspect-ratio wings pose a unique aerodynamic challenge. Often employed in small-scale flight applications, including package delivery (Golubev & Visbal 2012) and disaster relief (Daud *et al.* 2022), low-aspect-ratio wings are expected to operate in conditions that break the classical assumption of inviscid, attached flow. These wings are

† Email address for correspondence: lsmith1@ucla.edu

thus prone to a host of unsteady, often undesirable aerodynamic effects, including flow separation, vortex shedding and nonlinear oscillations in aerodynamic force (Shyy *et al.* 2007). At the same time, the compact footprint of these vehicles augments the impact of the wing tip vortex, imparting a large degree of downwash over a significant portion of the wing span (Jian & Ke-Qin 2004). The resulting flow field is tangled and complex: flow separation leads to the shedding of spanwise vortices, and these shed vortices undergo an intricate interaction with the wing tip. Such a three-dimensional, vortex-dominated flow field precludes accurate prediction with conventional aerodynamic theory (Bird & Ramesh 2021).

Partially because of this gap in understanding, there exists a growing body of literature concerned with the separated flow over aerodynamic bodies, with particular attention paid to the role of three-dimensionality. Many of these studies focus on spanwise periodic (or nominally two-dimensional) wings, and have produced detailed descriptions of the airfoil wake as a function of wing incidence, Reynolds number and planform geometry (Menon & Mittal 2020; Kurtulus 2021; Ribeiro *et al.* 2022). Collectively, these studies suggest that a separated wake exhibits a limit cycle oscillation up to a critical Reynolds number of $Re \approx 1000$, at which point spanwise instabilities initiate the route to chaos (Hoarau *et al.* 2003; Zhang & Lu 2009; He *et al.* 2017). While rich with fundamental insight, studies of spanwise periodic wings necessarily lack the presence of a wing tip, and thus have limited applicability to fully three-dimensional, low-aspect-ratio wings.

The simulation of finite wings, or those with a defined wing tip geometry, are more directly relevant to modern, small-scale flight application. In turn, computational efforts have begun to parse the interaction between a massively separated flow and a strong tip vortex. Taira & Colonius (2009) were among the first to explore this phenomena in the low-Reynolds-number regime, performing direct numerical simulation (DNS) over a sweep of aspect ratios and incidence angles at $Re = 300$. The authors found that the tip vortex, by virtue of its downwash, imparts a stabilising effect on leading-edge separation, while simultaneously promoting complex linkages among wake vortices. Subsequent studies would expand the parameter space significantly, partitioning the flow into steady, periodic and aperiodic regimes (Zhang *et al.* 2020; Pandi & Mittal 2023), while also laying the groundwork for control-oriented descriptions of the flow (Burtsev *et al.* 2022; Ribeiro, Yeh & Taira 2023).

The current work aims to address a persistent limitation in the existing literature: each study mentioned above was performed at a relatively low Reynolds number, with many studies limited to $Re < 1000$. In this work, we aim to understand how a change in Reynolds number affects the physical interplay between tip vortex and leading-edge separation. We also aim to bridge the gap between studies of finite wings at low Reynolds number, for which substantial progress has been made in the realm of stability and control, and studies of finite wings at higher, more turbulent Reynolds numbers (Devenport *et al.* 1996; Garmann & Visbal 2017). We accomplish these goals by performing high-fidelity computation over a sweep of Reynolds numbers in the range of $600 \leq Re \leq 10\,000$. The following sections will address how these simulations were performed, and how the resulting flow fields differ from their low-Reynolds-number counterparts.

2. Methodology

In this work, we consider high-fidelity numerical simulations of a finite, NACA 0012 wing at five values of the chord-based Reynolds number, $Re = U_\infty c/\nu$. Figure 1 provides an isometric view of our computational domain and serves as a problem statement for the current work. In this figure, we define the streamwise (x), vertical (y) and spanwise (z)

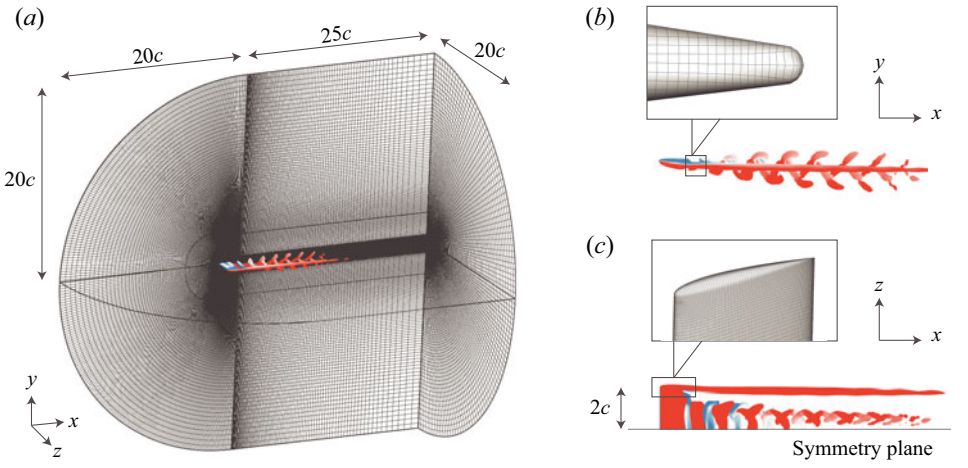

Figure 1. (*a*) The computational domain, (*b*) trailing-edge curvature and (*c*) wing tip geometry for the present simulations.

directions using Cartesian coordinates, and we place the origin $(0, 0, 0)$ at the leading edge of the wing root. Figure 1 also highlights several features of the wing surface geometry. For all simulations, we consider a semi-aspect-ratio $sAR = 2$ wing, outfitted with a rounded wing tip and a rounded trailing edge, at an incidence of $\alpha = 14^\circ$. We choose this specific combination of incidence and aspect ratio as a way of ensuring that both leading-edge separation and vertical downwash are present over a substantial portion of the wing planform.

For all five Reynolds numbers, we perform computations using the compressible flow solver *CharLES*, a finite-volume solver with second-order accuracy in space and third-order accuracy in time (Brès *et al.* 2017). We formulate each simulation as either a DNS ($Re \leq 2500$) or a large-eddy simulation (LES; $Re \geq 5000$), with the Vreman subgrid scale model providing turbulent closure for our LES (Vreman 2004). In both formulations, we prescribe a Dirchlet boundary condition ($U_\infty/a_\infty = 0.1$) at the inlet and farfield boundaries; a sponge boundary condition (with a spatial window of $x/c \in [15, 25]$) at the outlet boundary; and an adiabatic wall boundary condition at the airfoil surface. We impose a symmetry condition at the wing mid-span ($z = 0$) as a means of minimising our cell count. When advancing the simulation in time, we select a time step such that the local Courant number remains below $U_\infty \Delta t/\Delta x = 1$ throughout the entire domain.

Because we are interested in the separated flow regime, our flow field will exhibit characteristics similar to bluff body vortex shedding, and we expect to observe an increasingly broad spectrum of flow structures as we increase the Reynolds number. We thus generated multiple volumetric grids for this study to ensure sufficient resolution of the energy-containing scales. We build each mesh by first generating a structured grid along the airfoil surface, extending this grid as a two-cell-thick block along the streamwise extent of the wake, and space-marching the combined grid outward along the surface normal. We choose the resolution of our surface mesh, along with the growth rate of the space-marching procedure, such that each simulation is considered either a DNS ($Re \leq 2500$) or an LES ($Re \geq 5000$). Additional details regarding our choice of grid resolution, along with a quantification of the grid-dependence inherent to our results, can be found in the Appendix.

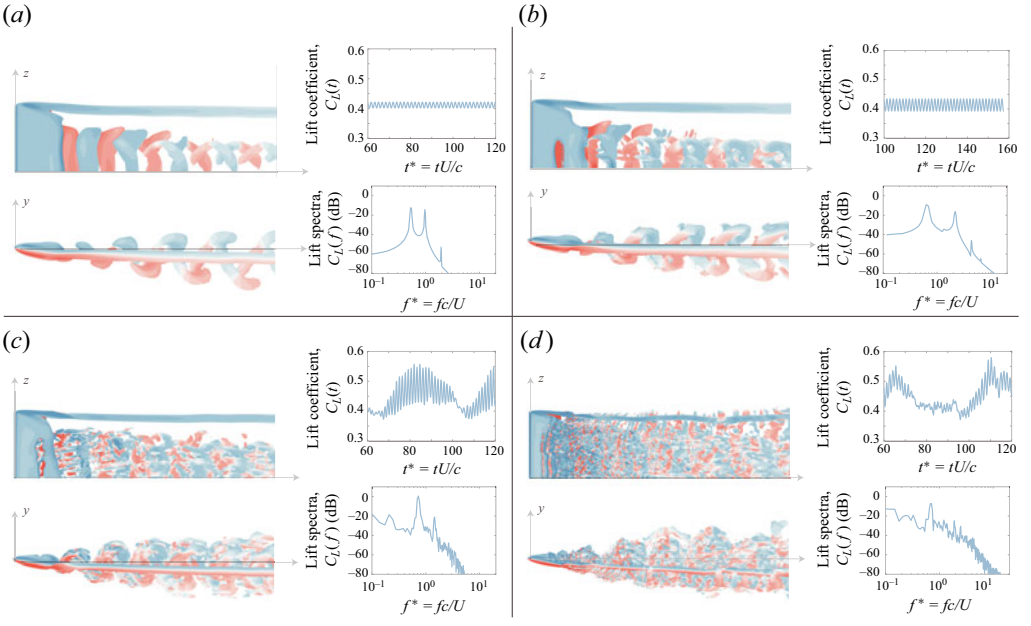

Figure 2. Instantaneous isocontours of Q-criterion, lift coefficient trace and lift spectra for (*a*) $Re = 600$, (*b*) 1000, (*c*) 2500 and (*d*) 10 000.

3. Results

We now examine the flow field produced by a low-aspect-ratio wing ($sAR = 2$) at constant incidence ($\alpha = 14^\circ$) over a sweep of Reynolds numbers ($600 \leq Re \leq 10\,000$). We begin by considering a qualitative overview of the flow as a function of Reynolds number, before focusing on the interaction between the tip vortex and shed wake. Figure 2 shows a series of flow field metrics intended to capture the scale, character and intensity of unsteady flow structures across our sweep of Reynolds numbers. Each subpanel of figure 2 includes three representations of the unsteady flow field: an instantaneous snapshot of Q-criterion, coloured by contours of spanwise vorticity (ω_z); a time history of the lift coefficient, integrated along the entire body of the wing; and a spectral description of the unsteady lift coefficient, computed via Welch's method. Note that when computing the lift spectra, we only include measurements collected at least 45 convective times beyond the simulation's impulsive start.

Looking at figure 2, we observe several striking changes in the character of the flow as we increase Reynolds number. We begin by noting that the $Re = 600$ case appears organised and coherent: we can visually identify shed vortices, the lift coefficient evolves periodically in time and the lift spectra is dominated by a single vortex shedding frequency (the Strouhal number) and its harmonics. The flow behaves similarly at $Re = 1000$, with only a slight increase in the magnitude of lift oscillations. As we move from $Re = 1000$ to $Re = 2500$, the flow undergoes a notable change, losing much of its qualitative coherence. While we can still identify shed vortices in the near-wing region, the wake at $Re = 2500$ is interspersed with small-scale shear linkages, and the lift spectra transitions to a more broadband distribution (while still exhibiting a minor peak at the Strouhal shedding frequency). This breakdown of the wake is intensified at $Re = 10\,000$, at which point shed vortices are almost entirely obscured by small-scale eddies.

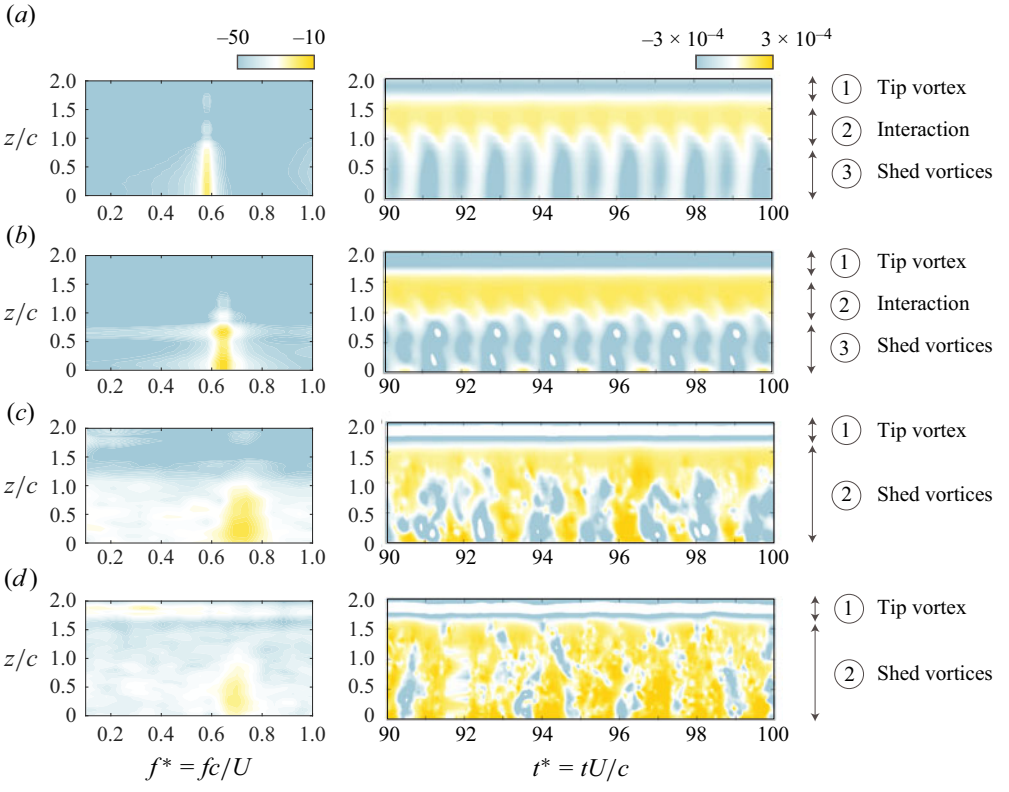

Figure 3. The pressure spectra (left) and instantaneous pressure (right) at $(x/c, y/c) = (3.0, -0.25)$ for (*a*) $Re = 600$, (*b*) 1000, (*c*) 2500 and (*d*) 10 000.

Figure 3 offers an alternate view of the airfoil at multiple Reynolds numbers. In this figure, we plot the signal from a pressure rake positioned downstream of the airfoil surface; the rake consists of 50 spanwise-aligned pressure probes at $(x/c, y/c) = (3.0, -0.24)$. The right column of figure 3 shows the temporal evolution of this pressure signal, while the left column describes its spectral composition as a function of spanwise position (z/c).

Echoing the flow field snapshots of figure 2, we observe a growing incoherence in the pressure signal as Reynolds number increases – an incoherence that appears to increase sharply between $Re = 1000$ and 2500. Whereas figure 3(*a*,*b*) exhibit clear spikes that can be linked to distinct flow structures (i.e. shed vortices, a tip vortex and a quasi-steady region in which the two interact), the remaining rows of figure 3 suggest a breakdown of these flow structures. Figure 3(*c*) shows the emergence of 'choppiness' in the structure of each pressure band, pointing towards the irregular, three-dimensional nature of passing vortices, whereas figure 3(*d*) sees this irregularity spread outboard, into the region of tip vortex interaction. The spectral character of the wake is also impacted by the increase in Reynolds number. The left column of figure 3 reveals that the wake's frequency content shifts to a higher frequency and dims in intensity, implying that the signal has drifted into aperiodicity.

Altogether, figures 2 and 3 suggest the presence of two vortex shedding regimes. In the first regime ($600 \leq Re \leq 1000$), the airfoil wake exhibits strong periodicity and its spatial structure can be partitioned into distinct regions. In the second regime

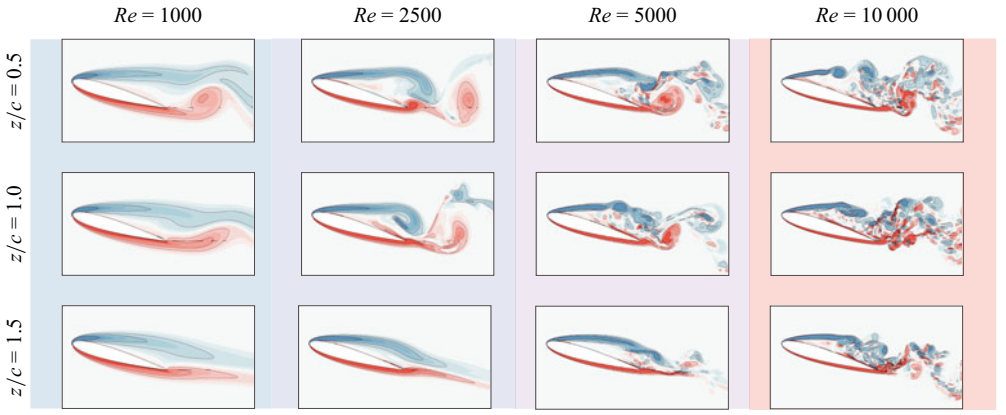

Figure 4. Slices of the spanwise vorticity field (ω_z) for a sweep of Reynolds numbers (rows) and spanwise locations (columns).

($2500 \leq Re \leq 10\,000$), these spatial regions break down, the structure of the wake becomes disorganised and broadband unsteadiness spreads from wing root to wing tip.

We now focus our attention on a specific aspect of the flow over a finite wing: the interplay between shed vortices, or those resulting from leading-edge separation, and the tip vortex that forms at the rounded edge of our wing. This interaction is key to the onset of wake disorganisation; while itself a quasi-steady flow feature, the tip vortex plays a crucial role in the onset of shear instability and vortex rollup (Huang & Lin 1995; Ribeiro *et al.* 2022). We begin by visualising the effect of Reynolds number on the leading-edge shear layer before reframing these effects in the context of the tip vortex.

Figure 4 shows instantaneous slices of the spanwise vorticity field (ω_z) collected in the near-wing portion of our computational domain. We organise this figure such that Re increases along each row, while z/c moves outboard along each column. Let us begin by considering the first row of figure 4, which shows the unsteady flow at $z/c = 0.50$. Looking specifically at the flow near the leading edge, we observe a clear trend: as we increase the Reynolds number, the leading-edge shear layer becomes thinner, and the onset of shear layer instability moves upstream. The $Re = 1000$ case exhibits only a minor accumulation of negative vorticity as it interacts with the trailing-edge vortex; by $Re = 2500$, the flow exhibits a clear rollup in a region just downstream of the trailing edge; and by $Re = 10\,000$, small-scale vortex rollup is visible as early as the airfoil mid-chord. The first row of figure 4 suggests that an increase in Reynolds number promotes the upstream rollup of spanwise vortices, which leaves the near-wing region prone to disorganisation.

Next, let us examine how these vortex structures change as we move closer to the wing tip. Consider the second column of figure 4, which shows the vorticity field (ω_z) at $Re = 2500$ over a sweep of spanwise locations. In the first row of this column, we observe the expected instability of the leading-edge shear layer, with vortex rollup occurring near the trailing edge. As we move down the column, we observe attenuation of this instability. In fact, the flow field at $z/c = 1.5$ exhibits a relatively stable shear layer for $Re = 2500$, with minimal indication of vortex rollup or complex unsteadiness. Moving to $Re = 10\,000$, vortex rollup is visible just beyond the midchord for all spanwise stations, but the degree of disorganisation is substantially more mild at $z/c = 1.5$ compared with regions closer to the root. In this sense, figure 4 suggests that the tip vortex imparts a stabilising effect on the leading-edge shear layer, an effect that grows more significant as we approach the

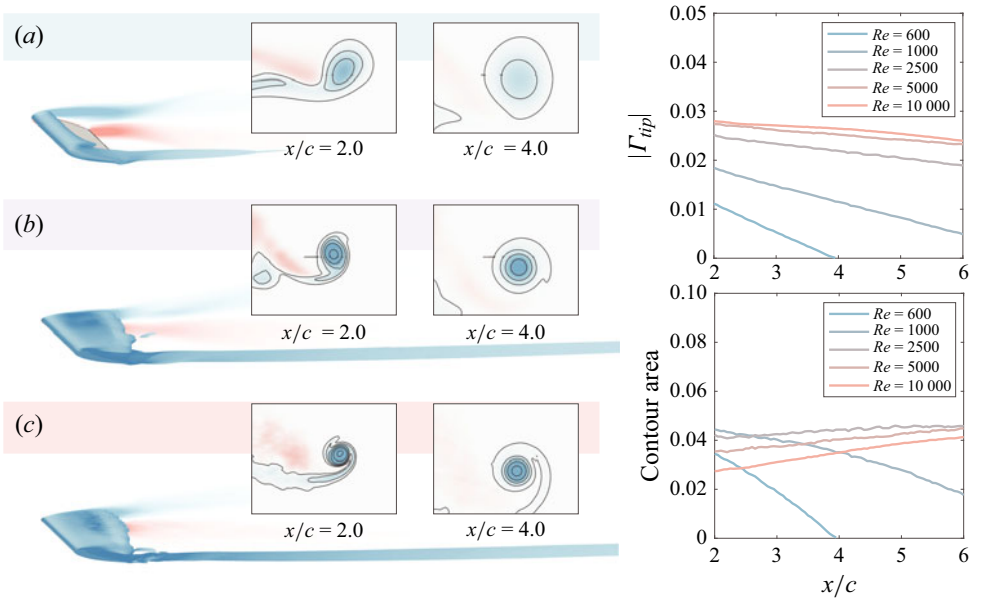

Figure 5. Spatial evolution of the tip vortex in the time-averaged flow field for (*a*) $Re = 600$, (*b*) 2500 and (*c*) 10 000.

wing tip. Such an observation can be attributed to the role of downwash in an aerodynamic flow: as we move closer to the tip, downwash becomes more severe and local incidence becomes more mild, ultimately leading to an attenuation of instability in the separated shear layer.

Broadly, figure 4 demonstrates that the local structure of the shed wake is strongly dependent on its proximity to the tip vortex, an observation that holds across all Reynolds numbers in the current study. Figure 5 expands upon this idea by quantifying the strength of the tip vortex. In this figure, we plot time-averaged isocontours of Q-criterion, along with planar snapshots of the streamwise vorticity field (ω_x), for a sweep of Reynolds numbers over $600 \leq Re \leq 10\,000$. We also track the circulation and planar area associated with a single isocontour; these two quantities are plotted on the right-hand side of figure 5. For both methods of visualisation, we observe a similar trend: as we increase the Reynolds number, the tip vortex grows in intensity and persistence, exhibiting reduced spatial dissipation beyond $Re = 1000$. This observation is supported by the left-hand side of figure 5, which exhibits more concentrated, higher intensity contours as the Reynolds number increases, and by the right-hand side of figure 5, which shows that the tip vortex maintains its strength and size for a substantially longer streamwise extent at Reynolds numbers beyond $Re = 1000$.

We thus arrive at one of the main conclusions of this work. That is, an increase in Reynolds number produces two seemingly opposing effects: (1) an increase in the likelihood of shear layer rollup for inboard regions of the wing; and (2) an increase in the strength and persistence of the tip vortex, which attenuates vortex rollup in outboard regions of the wing. This dichotomy provides a simple explanation for the regime changes observed in figure 2. At low Reynolds number ($Re \leq 1000$), the degree of shear instability is mild, and the strength of the tip vortex is enough to suppress vortex breakdown across the entirety of the wing span. Between $Re = 1000$ and 2500, the degree of instability grows to the point that inboard portions of the wing ($0 \leq z/c \leq 1.5$) transition to irregular, unsteady shedding, while outboard portions of the wing ($0.50 \leq z/c \leq 0.0$) remain quasi-steady.

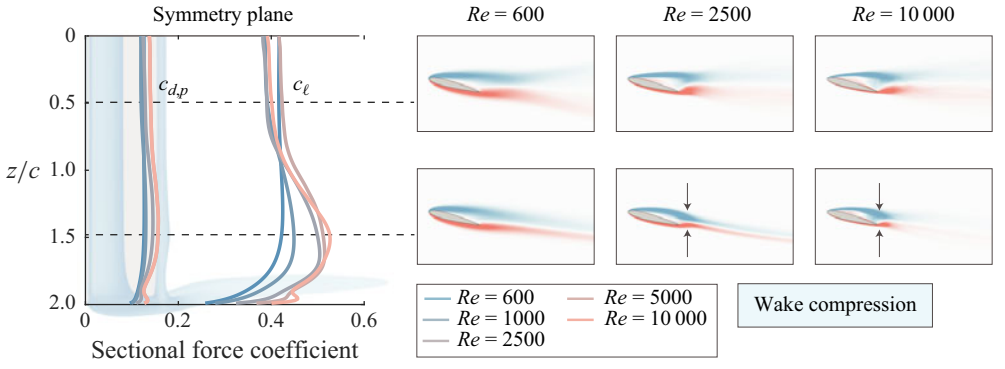

Figure 6. Spanwise distribution of the time-averaged lift coefficient (c_l) and pressure drag coefficient ($c_{d,p}$) for a sweep of Reynolds numbers. The insets show the mean spanwise vorticity field at specific spanwise locations.

By $Re = 10\,000$, the degree of shear instability outpaces the growing strength of the tip vortex, and small-scale vortex structures begin to emerge near the tip vortex, albeit gradually. Note that while outboard unsteadiness has just begun to emerge by $Re = 10\,000$, we expect the general structure of figure 2 to persist beyond $Re = 10\,000$. Previous studies (Garmann & Visbal 2017; Toosi *et al.* 2023) have reported a quasi-steady tip vortex, coupled with the widespread entrainment of small-scale vortex structures, at Reynolds numbers $O(10^5)$, suggesting that the gradual outboard spread of unsteadiness continues to higher Re.

The trend described above, wherein the tip vortex stabilises outboard portions of the wing, is particularly relevant to wings with a short span and has important implications on the production of aerodynamic force. Figure 6 plots the time-averaged lift and pressure-drag coefficients as a function of span for a sweep of Reynolds numbers, with insets showing the time-averaged vorticity field (ω_z) at select locations. In this figure, we observe a large, outboard spike in sectional lift coefficient for Reynolds numbers beyond $Re = 600$. While tip vortices are conventionally associated with a reduction in sectional lift, the presence of this spike is consistent with many of our observations thus far. For example, if we move along the bottom row of figure 6, we observe that vorticity is pulled closer to the airfoil surface with increasing Reynolds number, thus strengthening its contribution to vortex lift (Lee *et al.* 2012). We can, in turn, view the spanwise lift distribution as a reflection of the interplay between vortex rollup and local downwash; that is, shear instabilities concentrate vorticity into discrete structures, while downwash draws these structures closer to the wing surface.

Up to this point, we have limited our discussion of low-aspect-ratio wings to the interaction between the tip vortex and the leading-edge shear layer. While critical to the production of aerodynamic force, this interaction is constrained to the near-wing portion of the domain, and is only implicitly related to the behaviour of vortices as they move downstream. Thus, we next consider the three-dimensional structure of shed vortices over many convective times, augmenting our portrait of the airfoil wake with the details of its downstream structure.

Because our parameter space includes higher Reynolds numbers ($Re > 1000$), it can be difficult to visualise the structure of wake vortices via traditional techniques. We must instead rely upon some means of temporal, conditional averaging in order to parse the complex interactions that characterise the downstream wake. Here, we employ the dynamic mode decomposition (DMD) to accomplish this task. DMD operates by finding

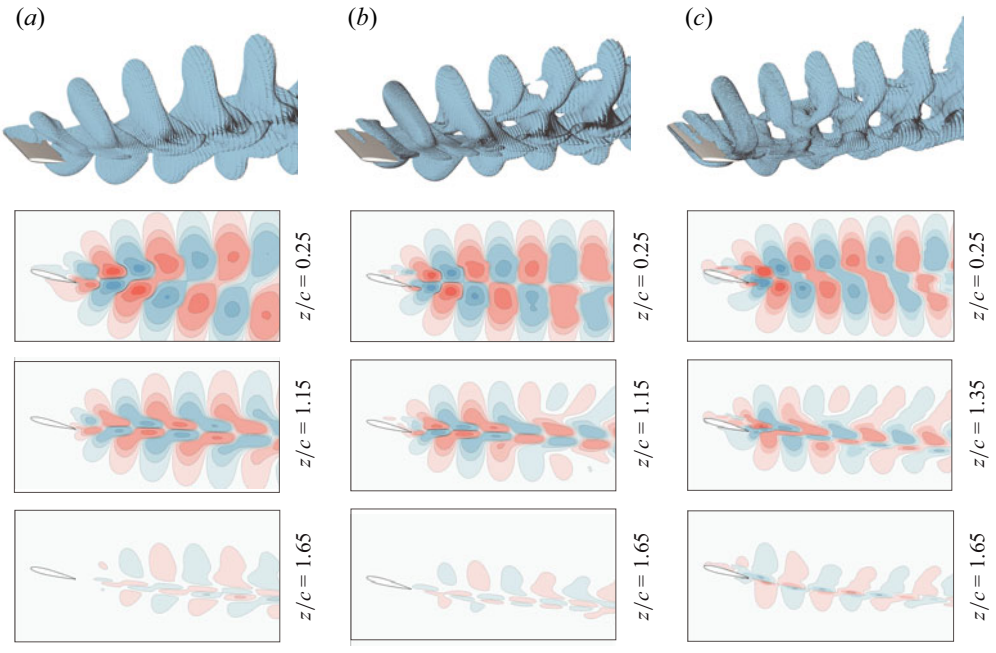

Figure 7. The three-dimensional DMD mode associated with the dominant vortex shedding frequency for (*a*) $Re = 600$, (*b*) $Re = 1000$ and (*c*) $Re = 2500$.

the best-fit linear operator for the discrete dynamical system governing the evolution of the flow; the eigenvectors of this linear operator are called 'modes' and represent recurrent spatial patterns in a time series of flow field snapshots (Kutz *et al.* 2016). Because DMD assumes a linear system, each of these modes can be linked to a discrete frequency.

With this in mind, figure 7 shows the dominant DMD mode for three representative Reynolds numbers, computed using streamwise velocity (u_x) as the state variable. For each case in this figure, we select the appropriate eigenvector by extracting a dominant vortex shedding frequency from the unsteady lift spectra (see figure 2) and matching this frequency with the nearest (purely imaginary) eigenvalue from DMD. Note that because the flow's aperiodicity grows with Reynolds number, we require an increasing number of snapshots to ensure convergence at higher Reynolds numbers. We thus incorporate 200 snapshots in the computation of the $Re = 600$ mode; 300 snapshots in the computation of the $Re = 1000$ mode; and 2000 snapshots for the computation of the $Re = 2500$ mode.

Let us begin by considering the DMD mode associated with our lowest Reynolds number. In figure 7(*a*), we observe a sequence of tube-like structures cascading through the wake of the airfoil, a common modal pattern associated with periodic vortex shedding and convection. Each of these tube-like structures resembles an *arch* in three-dimensional space. If we shift our attention downstream, these arches undergo substantial tilting and distortion over time, with outboard regions transitioning from a spanwise (z) alignment to more of a streamwise (x) alignment. The timing, behaviour and distortion of these tubes is closely linked to the impact of the tip vortex on the shed wake. Specifically, the arch-like structure of each tube is indicative of a strong spanwise gradient in downwash velocity, as outboard regions of each tube are subject to intense downwash from the tip vortex. Meanwhile, the streamwise tilting of each tube is indicative of a strong spanwise gradient in streamwise velocity, as outboard regions of each tube are disrupted by the axial velocity of the tip vortex.

We now examine how this arch structure changes with an increase in Reynolds number. Looking at figures 7(*b*,*c*), we still observe the familiar chain of arch-like modal structures, but with two primary differences compared with $Re = 600$. First, we note that the degree of streamwise vortex tilting (i.e. the rate at which each 'tube' is reoriented towards the x-axis) appears to increase as we increase the Reynolds number. This observation can be linked to the behaviour of the tip vortex described in figure 5. Because the strength and persistence of the tip vortex increases directly with the Reynolds number, each tube is subject to a sharper, more intense spanwise gradient, which persists over an increasingly large streamwise portion of the wake. In turn, the modal structures of figure 7(*b*,*c*) shows signs of streamwise tilting at significantly more upstream locations compared with figure 7(*a*).

Second, we note that the 'legs' of each tube, or the outboard regions in which each tube tilts rapidly toward the tip vortex, appear increasingly distinct as we move from figure 7(*a*,*b*). This observation implies that the 'interaction' region, over which shed vortices merge with the tip vortex, becomes increasingly compressed as we increase the Reynolds number. Such an observation aligns with the physics of the airfoil wake; in figure 3, we observed that the bounds of the 'interaction' region are pushed outboard as wake disorganisation casts a wider breadth.

All in all, the DMD modes of figure 7 indicate that an increase in Reynolds number produces two primary changes to the downstream structure of shed vortices: (1) an increase in the intensity of streamwise vortex tilting; and (2) an outboard shift in the region where this tilting is concentrated. These trends are consistent with our physical observations regarding the strength and persistence of the tip vortex, and demonstrate the close coupling between shed vortices and tip vortices observed across the current Reynolds number range.

4. Concluding remarks

In this work, we investigated the unsteady flow over a low-aspect-ratio ($sAR = 2$) wing at multiple values of the freestream Reynolds number ($600 \leq Re \leq 10\,000$). Our broad goal was to characterise the airfoil wake as it transitions from large-scale, periodic vortex shedding ($Re \approx 10^2$) to disorganisation and three-dimensionality ($Re \approx 10^4$), with an emphasis on the role of the wing tip vortex. Using a combination of DNS ($Re \leq 2500$) and LES ($Re \geq 5000$), we identified a regime change near $Re = 1000$, in which wake vortices break down, aerodynamic force becomes aperiodic, and disorganisation overtakes inboard portions of the airfoil wake. For $Re > 1000$, we find that an increase in Reynolds number promotes instability in the leading-edge shear layer, while also strengthening the wing tip vortex, which implicitly suppresses instability in outboard regions of the wing. The result is a gradual spread of fine-scale structures from the inboard, nominally two-dimensional portion of the wing, towards the outboard, tip-vortex-influenced portions of the wing. Collectively, these observations illuminate how a strong, persistent tip vortex impacts the structure of a transitioning shear wake, and lay the groundwork for a physical understanding of low-aspect-ratio wings in realistic, high-Reynolds-number conditions.

Acknowledgements. L.S. and K.T. wish to thank Dr. Daniel Garmann for thoughtful discussion on the dynamics of separated, aerodynamic flows.

Funding. L.S. and K.T. acknowledge the generous support of the US Air Force Office of Scientific Research (Grant No. FA9550-21-1-0174) and the US Department of Defense Vannevar Bush Faculty Fellowship (Grant No. N00014-22-1-2798).

Declaration of interests. The authors report no conflict of interest.

Re	$n_{airfoil}$	n_y	n_z	n_w	y_0^+	Cell count (10^6)
600	80	160	50	170	0.17	4.0
1000	120	200	75	260	0.14	11.4
2500	120	200	75	260	0.33	11.4
5000	160	250	105	345	0.31	26.5
10 000	160	250	105	345	0.59	26.5

Table 1. Geometric resolution parameters for each of the five Reynolds number cases.

Author ORCIDs.
Luke Smith https://orcid.org/0000-0002-3215-8422;
Kunihiko Taira https://orcid.org/0000-0002-3762-8075.

Appendix

In this appendix, we provide additional details regarding the set-up of our computational domain. We begin by noting that for all Reynolds numbers considered here, the resolution of our computational domain is governed by the following geometric parameters: the number of grid points allocated to the wing tangent ($n_{airfoil}$); the number of grid points allocated to the wing span (n_z); the number of grid points allocated to the wing normal (n_y); and the number of streamwise grid points allocated to the airfoil wake (n_w). Table 1 assigns values to these parameters for each of our five Reynolds number cases; this table also reports the value of our initial off-wall spacing (y_0^+) in viscous wall units. We choose the value of each parameter such that the average edge length within the near-wing mesh (i.e. the region corresponding to $-2.0 \leq x/c, y/c, z/c \leq 2.0$) roughly conforms to a set of grid spacing limitations. For $Re \leq 2500$, these limitations correspond to a DNS, i.e. $(\Delta x^+, \Delta y^+, \Delta z^+) \leq (2.5, 2.5, 5.0)$, while for $Re \geq 5000$, these limitations correspond to an LES, i.e. $(\Delta x^+, \Delta y^+, \Delta z^+) \leq (5.0, 5.0, 10.0)$. Note that for both DNS and LES cases, we select an initial off-wall spacing such that the innermost region near the wall ($y^+ < 5$) contains a minimum of six grid points.

Figure 8 collects the results of a grid-independence study undertaken to assess the accuracy of the mesh parameters reported above. In figure 8, each subplot corresponds to a separate Reynolds number, and shows isocontours of streamwise velocity, averaged over a temporal window of >50 convective time units. Each subplot also includes a running average of the lift coefficient, $C_L = 2F_y/\rho U_\infty^2 S$, as a means of visualising the flow's global convergence behaviour. For each Reynolds number, the label 'regular' corresponds to the level of grid refinement reported in table 1. When evaluating the grid independence of a given Reynolds number, we generate a new 'fine' and 'finer' grid by applying refinement uniformly across our four governing geometric parameters. Each subsequent level of grid refinement roughly doubles the total cell count of the mesh. Note that because of a prohibitively high cell count, we limit the $Re = 10\,000$ case to a single iteration of grid refinement.

Figure 8 reveals that our time-averaged solution exhibits minimal sensitivity to successive levels of grid refinement. The isocontour lines of figure 8(*a*,*b*) are nearly identical to one another, suggesting that a 'regular' grid provides sufficient resolution for the $Re = 600$ and $Re = 2500$ cases. The downstream isocontour lines begin to deviate from one another at $Re = 10\,000$, likely owing to the flow's increasing spatiotemporal irregularity, but the differences are slight, and even for $Re = 10\,000$, the aerodynamic force

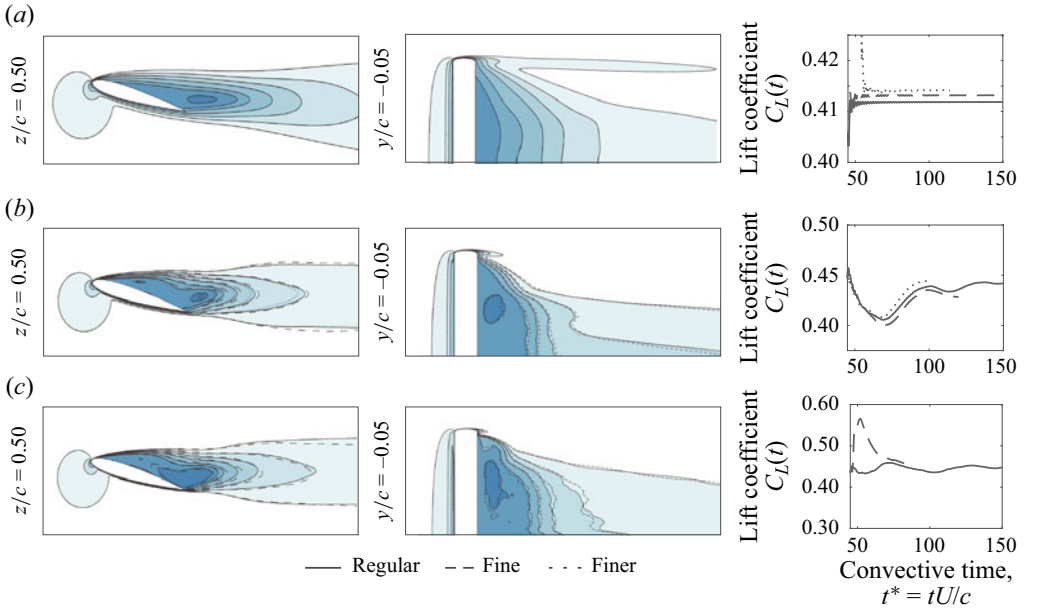

Figure 8. The effect of grid resolution on the time-averaged, streamwise velocity field (left and centre columns) and the time-averaged lift coefficient (right column). (*a*) $Re = 600$, (*b*) $Re = 2500$ and (*c*) $Re = 10\,000$.

appears to converge after a few dozen convective times. We thus consider our solution spatially converged; the results presented throughout this work correspond to the 'regular' grids outlined in table 1.

References

Bird, H.J.A. & Ramesh, K. 2021 Unsteady lifting-line theory and the influence of wake vorticity on aerodynamic loads. *Theor. Comput. Fluid Dyn.* **35**, 609–631.

Brès, G.A., Ham, F.E., Nichols, J.W. & Lele, S.K. 2017 Unstructured large-eddy simulations of supersonic jets. *AIAA J.* **55** (4), 1164–1184.

Burtsev, A., He, W., Zhang, K., Theofilis, V., Taira, K. & Amitay, M. 2022 Linear modal instabilities around post-stall swept finite wings at low Reynolds number. *J. Fluid Mech.* **944**, A6.

Daud, S.M.S.M., Yusof, M.Y.P.M., Heo, C.C., Khoo, L.S., Singh, M.K.C., Mahmood, M.S. & Nawawi, H. 2022 Applications of drone in disaster management: a scoping review. *Sci. Justice* **62** (1), 30–42.

Devenport, W.J., Rife, M.C., Liapis, S.I & Follin, G.J. 1996 The structure and development of a wing-tip vortex. *J. Fluid Mech.* **312**, 67–106.

Garmann, D.J. & Visbal, M.R. 2017 Analysis of tip vortex near-wake evolution for stationary and oscillating wings. *AIAA J.* **55** (8), 2686–2702.

Golubev, V.V. & Visbal, M.R. 2012 Modeling MAV response in gusty urban environments. *Intl J. Micro Air Veh.* **4** (1), 79–92.

He, W., Gioria, R.S., Perez, J.M. & Theofilis, V. 2017 Linear instability of low Reynolds number massively separated flow around three NACA airfoils. *J. Fluid Mech.* **811**, 701–741.

Hoarau, Y., Braza, M., Ventikos, Y., Faghani, D. & Tzabiras, G. 2003 Organized modes and three-dimensional transition to turbulence in the incompressible flow around a NACA0012 wing. *J. Fluid Mech.* **496**, 63–72.

Huang, R.F. & Lin, C.L. 1995 Vortex shedding and shear-layer instability of wing at low-Reynolds numbers. *AIAA J.* **33** (8), 1398–1403.

Jian, T. & Ke-Qin, Z. 2004 Numerical and experimental study of flow structure of low-aspect-ratio wing. *J. Aircraft* **41** (5).

KURTULUS, D.F. 2021 Vortex flow aerodynamics behind a symmetric airfoil at low angles of attack and Reynolds numbers. *Phys. Rev.* E **79**, 045306.

KUTZ, J.N., BRUNTON, S.L., BRUNTON, B.W. & PROCTOR, J.L. 2016 *Dynamic Mode Decomposition: Data-driven Modeling of Complex Systems*, 1st edn. Society for Industrial and Applied Mathematics.

LEE, J.-J., HSIEH, C.-T., CHANG, C.C. & CHU, C.-C. 2012 Vorticity forces on an impulsively started flat plate. *J. Fluid Mech.* **694**, 464–492.

MENON, K. & MITTAL, R. 2020 Aerodynamic characteristics of canonical airfoils at low Reynolds numbers. *AIAA J.* **58** (2), 977–980.

PANDI, J.S. & MITTAL, S. 2023 Streamwise vortices, cellular shedding, and force coefficients on a finite wing at low Reynolds number. *J. Fluid Mech.* **958**, A10.

RIBEIRO, J.H.M., YEH, C. & TAIRA, K. 2023 Triglobal resolvent analysis of swept-wing wakes. *J. Fluid Mech.* **954**, A42.

RIBEIRO, J.H.M., YEH, C., ZHANG, K. & TAIRA, K. 2022 Wing sweep effects on laminar separated flows. *J. Fluid Mech.* **950**, A23.

SHYY, W., LIAN, Y., TANG, J., VIIERU, D. & LIU, H. 2007 *Aerodynamics of Low Reynolds Number Flyers*, 1st edn. Cambridge University Press.

TAIRA, K. & COLONIUS, T. 2009 Three-dimensional flows around low-aspect-ratio flat-plate wings at low Reynolds numbers. *J. Fluid Mech.* **623**, 187–207.

TOOSI, S., PEPLINSKI, A., SCHLATTER, P. & VINUESA, R. 2023 The impact of finite span and wing-tip vortices on a turbulent NACA0012 wing. arXiv:2310.10857

VREMAN, A. 2004 An eddy-viscosity subgrid-scale model for turbulent shear flow: algebraic theory and applications. *Phys. Fluids* **16**, 3670.

ZHANG, K., HAYOSTEK, S., AMITAY, M., HE, W., THEOFILIS, V. & TAIRA, K. 2020 On the formation of three-dimensional separated flows over wings under tip effects. *J. Fluid Mech.* **895**, A9.

ZHANG, N.L.J. & LU, X. 2009 Route to a chaotic state in fluid flow past an inclined plate. *Phys. Rev.* E **79**, 045306.